2020 IEEE/RSJ International Conference on Intelligent Robots and Systems (IROS)
October 25-29, 2020, Las Vegas, NV, USA (Virtual)

An SEM-Based Nanomanipulation System for Multi-Physical Characterization of Single InGaN/GaN Nanowires

Juntian Qu, Renjie Wang, Peng Pan, Linghao Du, Zetian Mi, Yu Sun, and Xinyu Liu*

***Abstract*— Functional nanomaterials possess exceptional multi-physical (e.g., mechanical, electrical and optical) properties compared with their bulk counterparts. To facilitate both synthesis and device applications of these nanomaterials, it is highly desired to characterize their multi-physical properties with high accuracy and efficiency. The nanomanipulation techniques under scanning electron microscopy (SEM) has enabled the testing of mechanical and electrical properties of various nanomaterials. However, the seamless integration of mechanical, electrical, and optical testing techniques into an SEM for triple-field-coupled characterization of single nanostructures is still unexplored. In this work, we report the first SEM-based nanomanipulation system for high-resolution mechano-optoelectronic testing of single semiconductor InGaN/GaN nanowires (NWs). A custom-made optical measurement setup was integrated onto a four-probe nanomanipulator inside an SEM, with two optical microfibers actuated by the nanomanipulator for NW excitation and emission measurement. A conductive tungsten nanoprobe and a conductive atomic force microscopy (AFM) cantilever probe were integrated onto the nanomanipulator for electrical nanoprobing of single NWs for electroluminescence (EL) measurement. The AFM probe also served as a force sensor for quantifying the contact force applied to the NW during nanoprobing. Using this unique system, we examined, for the first time, the effect of mechanical compression applied to an InGaN/GaN NW on its optoelectronic properties.**

I. Introduction

The last two decades have witnessed the extensive research on nanomaterials by virtue of their exceptional promise in science and technology. Due to the superior physical properties and unique nanoscale morphologies, nanomaterials have been widely used for a variety of applications such as next-generation electronics [1], nanocomposite synthesis, sustainable energy [2], biosensing [3] and photonics [4]. The mechanical, electrical, optical, and field-coupled (e.g., electromechanical, optoelectronic, and opto-electromechanical) properties of these nanomaterials play critical roles in their practical applications; thus, the experimental characterization of these properties is thus of major concern from the perspective of both nanomaterial synthesis and device applications.

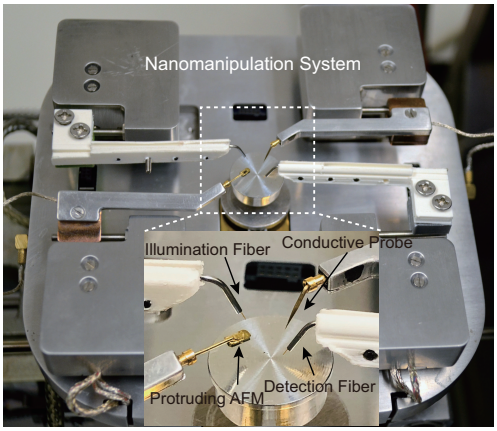

Fig. 1. SEM-based nanomanipulation system with the integration of multi-physical characterization end-effectors.

Among various experimental techniques employed for nanomaterial characterization, emerging nanomanipulation techniques under scanning electron microscopy (SEM) have been applied to characterizing the mechanical, electrical, and electromechanical properties of different types of nanomaterials and nanostructures [5], [6]. Comparing to the atomic force microscopy (AFM)-based nanomanipulation techniques, the involvement of an SEM provides vision feedback with a fast frame rate for imaging the nanostructures with high resolution and for monitoring and guiding the system for *in-situ* manipulation and characterization of single nanostructures [7].

With the rapid advances of optical and optoelectronic nanodevices, the optical and optoelectronic characterization of nanostructures become more and more widely used for the purpose of providing experimental guidelines for nanomaterial synthesis and improving the nanodevice performance. For optical characterization, only a few studies on cathodoluminescence (CL) characterization of nanomaterials [8], [9] were carried out in SEM. For optoelectronic characterization, SEM was only utilized for focused ion beam (FIB)-assisted metal contact deposition [10]; the major characterization processes were still performed in the ambient environment. The lack of SEM-based optical characterization is mainly due to the limited space of SEM chamber, which leads to the technical challenge of integrating optical components such as sizeable paraboloidal mirrors for effective light collection [11].

To perform optical characterization in SEM, efficient

Research supported by National Sciences and Engineering Research Council of Canada, Canada Research Chairs Program, and by the University of Toronto.

Juntian Qu, Peng Pan, Linghao Du, Yu Sun, and Xinyu Liu are with Department of Mechanical and Industrial Engineering, University of Toronto, Toronto, Ontario, Canada, M5S 3G8.

Juntian Qu, Peng Pan, and Xinyu Liu are also with Department of Mechanical Engineering, McGill University, Montreal, Quebec, Canada, H3A 0C3.

Juntian Qu is also with Department of Mechanical Engineering, Tsinghua University, Beijing, China, 100084, funded by "Shuimu Tsinghua Scholar" Program.

Renjie Wang and Zetian Mi are with Department of Electrical and Computer Engineering, McGill University, Montreal, Quebec, Canada, H3A 0C3.

Zetian Mi is also with Department of Electrical Engineering and Computer Science, University of Michigan, Ann Arbor, MI, United States, 48109.

*Corresponding author: xyliu@mie.utoronto.ca

light collection and luminescence detection are necessary. A sizeable paraboloidal mirror was employed in an SEM setup [11] for light collection in CL testing; however, due to the limited space of the SEM chamber, the mirror blocked most other detectors and did not allow electrical nanoprobe integration, thus hindering the simultaneous injection and measurements of electrical and optical signals into and from the nanomaterial. To address this issue, space-saving optical microfibers [9] were integrated into the SEM chamber for *in-situ* optoelectronic characterization of semiconductor nanowires. However, the experimental setup does not possess force sensing capability to quantify contact forces applied to the nanostructures for investigating the mechanical effect on the material's optoelectronic properties. Therefore, based on above discussions, it is highly desired to develop an SEM-based *in-situ* multi-physical characterization system capable of characterizing the multi-field (mechanical, electrical, and optical)-coupled properties of single nanomaterials.

In this paper, we report the development of the first SEM-based nanomanipulation system, which integrates mechanical, electrical, and optical measurement capabilities, for opto-electro-mechanical characterization of single one-dimensional (1D) nanowires. Through seamless integration of end-effectors capable of mechanical, electrical, and optical measurements, we developed experimental strategies for performing single-field and three-field-coupled testing of single nanowires, and calibrated the testing performance of each single-field characterization module. As a demonstration, we carried out opto-electro-mechanical testing of semiconductor InGaN/GaN NWs using the developed system, and experimentally quantified, for the first time, the effect of mechanical compression on the electroluminescence (EL) property of single InGaN/GaN NWs. The developed nanomanipulation system will greatly facilitate the multi-physical testing of semiconductor nanomaterials and thus expedite their synthesis parameter optimization processes and optoelectronic device applications.

II. Nanomanipulation System Development

A. System Overview

As shown in Fig. 1, the nanomanipulation system mainly consists of an SEM (SU3500, Hitachi) and a nanomanipulator with four closely-loop controlled nanopositioners (LF-2000, Toronto Nanoinstrumentation Inc.) mounted inside the SEM chamber. One Pt-coating conductive tungsten nanoprobe (ST-20-0.5, GGB Industries), one Pt-coating conductive atomic force microscope (AFM) cantilever probe with a protruding tip (ATEC-FM, NanoAndMore Corp.), and two optical micro-fibers (Accu-Glass Products Inc.) are individually mounted on the four nanopositioners, with the nanoprobe and AFM probe arranged along one diagonal direction and the two optical micro-fibers along the other diagonal direction.

The nanomanipulation system contains necessary components for operation in three single-field testing modes: (i) the electrical testing mode, (ii) the optical testing mode, and (iii) the mechanical testing mode. With the seamless integration of all the testing components and the development of the corresponding techniques, the system is capable of executing single-field and triple-field-coupled characterization tasks.

The Pt-coated tungsten nanoprobe and the AFM cantilever probe can be used for *in-situ* electrical nanoprobing of nanomaterials such as the as-grown single NWs on its growth substrate. Owing to its protruding tip visible from the SEM top view, the AFM cantilever probe can be guided by the SEM vision to contact the top surface of a single NW, without requiring the SEM sample stage to be tilted for observing the side view of the probe and the NW sample. For applying an electrical voltage/current to a NW sample, our system adopts *in-situ* two-point electrical nanoprobing rather than the conventional electron-beam lithography (EBL)-patterned electrode contacts, which avoids chemical treatment of the NW sample during EBL [12]. Through SEM visual guidance, the two optical micro-fibers can be precisely positioned to the proximity of a single NW for optical excitation and emission measurement. Besides, the protruding AFM probe can also serve as a high-resolution force sensor for contact force measurement during nanoprobing, which, in combination with the SEM-vision-based displacement measurement, enables mechanical characterization and stimulation (by applying strain/stress) of single NWs.

The major merit of this multi-physical characterization system is the flexibility of combining different types of end-effectors for different tasks. By combining both the emission measurement micro-fiber and the two conductive probes, we can perform optoelectronic (EL) characterization of a single NW, where the injection current can be applied to the NW using the two conductive probes and the resulting optical emission can be simultaneously measured by the optical micro-fiber. Moreover, this system can also be extended to triple-field-coupled (opto-electro-mechanical) characterization. For the triple-field coupled characterization, a single semiconductor NW is compressed by the AFM probe from the top at a desired contact force level, and the effect of the induced NW stress/strain on its EL property is quantified by the two conductive probes and the emission measurement optical micro-fiber. In this operation, the conductive AFM probe serves as both the electrical nanoprobe and the force-sensing end-effector. In the following sections, we will introduce the electrical, optical and mechanical characterization modules of the developed nanomanipulation system.

B. Electrical Characterization Mode

In the electrical testing mode, the system functions as an two-point electrical nanoprobing setup. In a previous work [13] , we have performed a systematic investigation of the experimental strategies for reducing the contact resistance between the conductive nanoprobe and the sample for *in-situ* nanomaterial probing without requiring metal electrode patterning. The details of the two-point nanoprobing protocol can be found in [13]. Based on the established protocol, the following SEM imaging parameters were used during vision-guided nanoprobing to reduce the e-beam-induced contaminant deposition and thus minimize the probe-sample

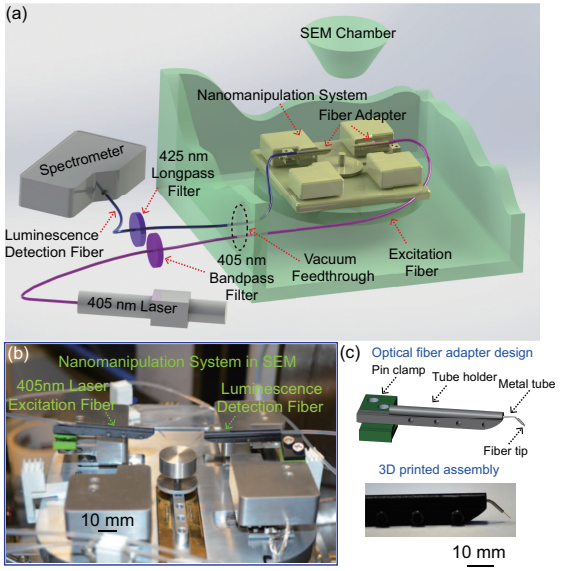

Fig. 2. SEM-based optical characterization module. (a) Schematic figure. (b) Photograph of optical characterization module with integrated dual optical fibers. (c) Photograph of optical fiber adapter.

contact resistance: (i) magnification = 9000×, (ii) spot size = 2.8, and (iii) acceleration voltage = 6 kV.

C. Optical Testing Mode

1) Optical Setup Design: In the optical testing mode, the nanomanipulation system employs the space-saving optical micro-fibers (vs. the conventional sizeable paraboloidal mirrors) for laser excitation and nanomaterial emission measurement. Figure 2(a) shows the schematic diagram of the optical characterization setup. A 405 nm collimated diode laser (LRD-0405-PFR-00500-05, Laserglow Technologies) was chosen as the optical excitation source, and the laser beam was guided into the SEM chamber through two multimode optical micro-fibers: one 100 μm UV/VIS bare polished fiber (112550, Accu-Glass Products Inc.) inside the SEM vacuum chamber (the vacuum side) and another 100 μm UV/VIS PMMA-encapsulated fiber (112552, Accu-Glass Products Inc.) outside the SEM chamber (the air side). A customized vacuum feedthrough was mounted on a port of the SEM chamber for connecting the two micro-fibers and coupling the laser beam from outside to inside of the chamber. To protect the fragile thin bare micro-fiber in the SEM chamber, a soft tube of 150 μm inner diameter (ID) was utilized to sheath the vacuum-side bare fiber. Finally, to complete the excitation loop setup, a 405 nm bandpass filter (OD4, Edmund Optics) was set in the path of air-side micro-fiber for selectively passing the 405 nm excitation signal.

To detect the optical emission from a nano-sample, two optical micro-fibers of the same type (wavelength range: 200-800 nm) were selected for mounting at both the air and vacuum sides of the SEM. The selection of the visible wavelength range meets the requirement of photo- and electroluminescence measurements of the InGaN/GaN NWs. Another customized vacuum feedthrough was mounted on the same SEM chamber port for connecting the micro-fibers and pass through the collected sample emission signal to

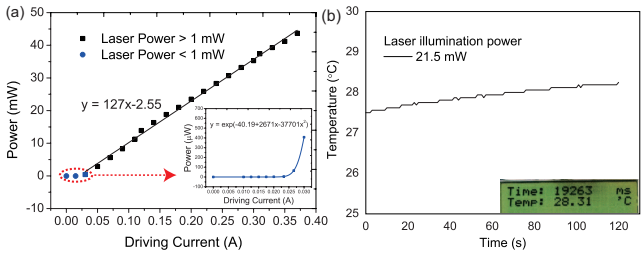

Fig. 3. Optical characterization module calibrations. (a) Illumination power. (b) Laser illumination impact. Inset: LED display of real-time temperature monitering.

outside of the SEM chamber. The end of air-side emission measurement micro-fiber was connected with a high-precision spectrometer (Ocean Optics, QE Pro-FL) with a back-thinned, TE-cooled CCD detector for luminescence measurement. To isolate the detected luminescence signal from the 405 nm excitation signal, a 425 nm longpass filter (OD4, Edmund Optics) was placed in the air-side detection path for filtering out any 405 nm signal.

A technical challenge for integration of the optical characterization setup was how to mount the two thin flexible bare micro-fiber tips onto the two nanopositioners and achieve fixed light excitation and detection angles. As shown in Fig. 2(c), we designed an optical micro-fiber adapter to stably mount a bare micro-fiber onto the nanopositioner. The flexible optical micro-fiber tip was firstly inserted into a customized metal tube with a 45° bending angle, and the metal tube was then inserted into the 150 μm ID protection tube. A 3D-printed tube holder was fabricated to immobilize the protection tube, and a custom-made pin clamp was integrated at the end of the tube holder for firmly clamping it onto the output pin shaft of the nanopositioner. This adapter design provides stable mounting of the two micro-fibers onto the two nanopositioners, and also allows the micro-fiber position and bending angle to be readily adjusted by changing the clamp position on the metal pin of the nanopositioner and the bending angle of the metal tube, respectively. Fig. 2(b) shows the laser excitation micro-fiber and emission measurement micro-fiber stably mounted on the nanomanipulator.

2) Optical Setup Calibration: To quantify the output illumination power at the excitation micro-fiber tip, we calibrated the entire excitation loop and obtained the data of total output power at the micro-fiber tip vs. driving current of the laser source. A digital optical power meter (PM100D, Thorlabs) with a 200-1000 nm photodiode power sensor (S120VC, Thorlabs) was utilized for this task, with the sensing probe of the meter covering the whole excitation fiber tip to minimize the energy loss during measurement. The calibration curve is shown in Fig. 3(a). One can observe a dead zone in the driving current range of less than 0.024 A, beyond which the laser power and driving current have a nonlinear correlation until 0.03 A [inset of Fig. 3(a)]. For any driving current over 0.03 A, the corresponding output laser power at the micro-fiber tip is linearly proportional to the driving current of the laser source. The maximum output laser power from the microfiber tip was 43.7 mW at the driving current of 0.37 A [Fig. 3(a)].

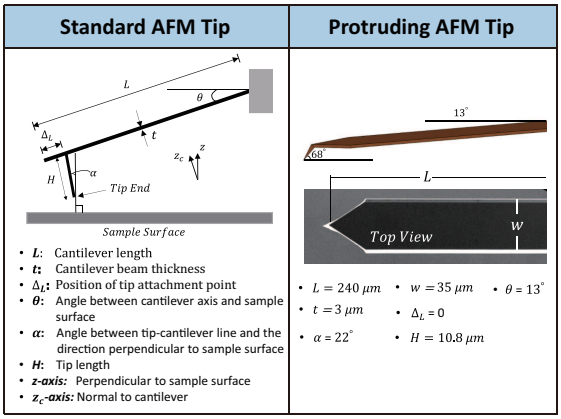

Fig. 4. Two types of AFM cantilever tip geometry: the standard AFM tip and the protruding AFM tip.

As temperature is a crucial factor that affects the optoelectronic properties (e.g., band gap, absorption of the incident radiation) of semiconductor nanomaterials, we also calibrated the sample temperature change induced by the e-beam and laser illumination in the enclosed SEM vacuum chamber (vacuum level: $\sim 3.33 \times 10^{-4}$ Pa). An digital temperature sensor (TMP 102, Sparkfun Electronics) was mounted onto the sample holder of the nanomanipulation system to measure the temperature rise after a certain period of e-beam illumination and laser excitation. It was verified that the e-beam illumination has no obvious impact on the sample holder temperature for 2 min continuous irradiation. Fig. 3(b) shows the temperature rise curve during 2 min continuous laser illumination at the power of 21.5 mW (which will be used for InGaN/GaN NW testing). Due to the slow thermal convection rate in the enclosed vacuum chamber, we observed a $\sim$0.5°C temperature rise after 2 min continuous laser illumination. As the nano-sample emission measurement is usually completed within 1 min, and the corresponding temperature rise of $\leq$0.3°C [Fig. 3(b)] will not significantly affect the optoelectronic property of the sample.

D. Mechanical Testing Mode

In the mechanical testing mode, the system employs the protruding AFM probe tip to contact the top surface of a single NW at different desired contact force level for investigation of the mechanical impact on the optical or optoelectronic property of of the NW. Due to its protruding shape [right of Fig. 4], the AFM probe tip is visible from the SEM top view and it is much easier to visualize the contact between the protruding tip and the NW top surface than a conventional AFM tip that hides beneath the cantilever beam during operation [left of Fig. 4]. Thus, we can readily establish stable contact between the AFM probe tip and the NW top surface. In this type of manipulation, the protruding AFM tip serves both a force sensor for contact force measurement and an electrical probe for optoelectronic characterization of the NW.

The protruding AFM probe was mounted onto the nanopositioner with three degrees of freedom (DOF; i.e., *x*-*y*-*z*) with a positioning resolution of 0.1 nm along each axis. To

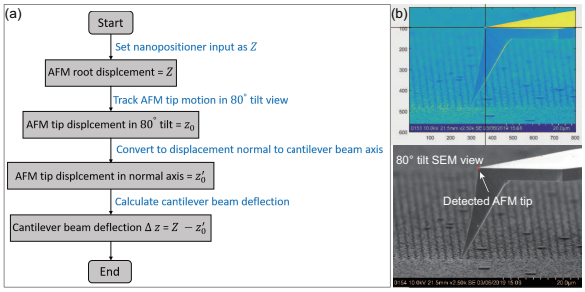

Fig. 5. Vision-based Tracking of Cantilever Beam Deflection. (a) Flow diagram. (b) Vision tracking of AFM tip motion in 80 ° tilting plane.

quantify the force applied to a NW by the AFM tip, the AFM cantilever beam deflection needs to be detected. However, from the SEM top view, the cantilever beam deflection cannot be visualized. In order to visually measure the cantilever beam deflection, we mounted the NW sample onto a 90° tilt holder. For better visualizing the probe tip-NW contact, the SEM stage was tilted at 10°. Equivalently, the NWs sample was tilted at 80° relative to the original horizontal plane [see SEM photographs in Fig. 5(b)]. With the NW-tilting setup, an experimental protocol was developed to calculate the AFM contact force on the top surface of a single NW, which includes three steps: (i) vision-based measurement of the cantilever beam deflection, (ii) stiffness tilt correction, and (iii) longitudinal torque correction.

1) Vision-based Tracking of Cantilever Beam Deflection: During nanoprobing of a NW, the AFM cantilever beam deflection can be calculated as the displacement difference between the root of cantilever beam and the AFM tip. As the cantilever root is firmly connected with the nanopositioner, its displacement was read out as the nanopositioner displacement, Z. In the 80°-tilt SEM view, we tracked the AFM tip displacement through a simple corner detection algorithm [Fig. 5(b)] and obtained the AFM tip displacement, z_0. Denote the tip displacement normal to the cantilever beam axis as $z_0^{'}$, and we calculated $z_0^{'} = z_0 / \sin 80°$. Then the cantilever beam deflection Δz can be calculated as $\Delta z = Z - z_0^{'}$. The whole flow of measuring the AFM cantilever beam deflection is shown in Fig. 5(a).

2) Stiffness Tilt Correction: After obtaining the cantilever beam deflection, in order to accurately quantify the contact force at the AFM tip, it is necessary to accurately calibrate the stiffness of the cantilever. During NW probing, the AFM cantilever was inclined at 13° (left of Fig 6) to allow its tip to access the sample top surface without allowing the cantilever holder (at its root) contact the sample substrate. Since the cantilever tilting angle affects the effective stiffness of the AFM cantilever, the cantilever beam stiffness in the tilting setup should be corrected based on the tilting angle [14].

The relationship between the cantilever effective stiffness and the tilting angle θ has been experimentally verified in a previous study using a microfabricated AFM cantilever [14]. The effective stiffness was determined to be $k_z = k_c / \cos^2 \theta$, where k_c is the intrinsic stiffness perpendicular to the long axis of the cantilever. Detailed schematic illustration of the tilting setup and effective stiffness correction is shown in

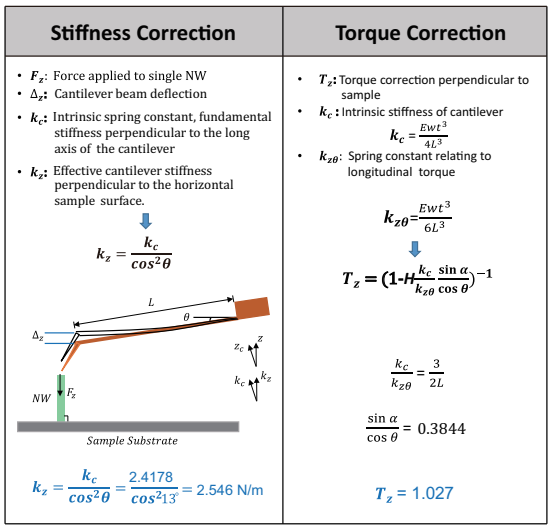

Fig. 6. Calculation of stiffness tilt and longitudinal torque corrections.

Fig. 6 (left). The intrinsic stiffness of the AFM cantilever beam was determined to be 2.4178 N/m using the thermal tune method [15] on a commercial AFM machine (Bioscope Resolve, Bruker). The effective stiffness of the protruding AFM cantilever in the 13° tilting setup was finally calculated to be 2.546 N/m.

3) Torque Correction: According to a general theoretical model [16], we can derive the applied AFM tip force (F_z in the left of Fig. 6) normal to the sample surface to be $F_z = k_z \Delta z T_z$, where k_z is the effective cantilever stiffness normal to the sample surface, Δz the obtained cantilever deflection, T_z the induced AFM tip torque correction factor in the presence of cantilever tilt [16]. Detailed derivation and calculation of T_z can be found in Fig. 6(right). For our 13°-tilted protruding AFM tip, the torque correction factor T_z was calculated to be 1.027.

III. Opto-Electromechanical Testing of InGaN/GaN Nanowires

Single InGaN/GaN NWs exhibit excellent light emission characteristics and have been applied to fabricate high-performance optoelectronic devices such as white light-emitting diodes (LEDs) [17] and deep-UV laser sources [18]. For packaging vertically-grown InGaN/GaN NW forests into a LED, a transparent indium tin oxide (ITO) electrode needs to be applied on top surfaces of the NWs to form a top-bottom electrode pair for current injection. This packaging process imposes mechanical strain and stress to the NWs, which may affect the optoelectronic properties of the NWs and thus the performance the fabricated LEDs. To date, there is no experimental study on how the mechanical effect of the NW packaging condition affect the optoelectronic properties of the NWs. Leveraging the unique capability of our system for triple-field-coupled testing of single NWs, we performed, for the first time, the mechano-optoelectronic characterization of single InGaN/GaN NWs.

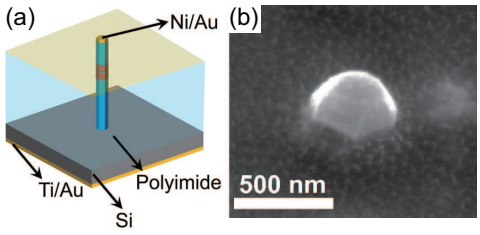

Fig. 7. Sample for EL test. (a) Schematic of a single InGaN/GaN NW LEDs on Si substrate. (b) Top-view SEM image of the exposed p-GaN nanowire top-surface after polyimide passivation and dry etching.

A. Sample Preparation

As schematically shown in Fig. 7(a), our InGaN/GaN NW samples were vertically grown on a Si substrate through a custom-made molecular beam epitaxy (MBE) process [19], and consisted of $\sim$ 0.45 μm n-GaN on the bottom, six InGaN/GaN quantum dot nanolayers in the middle, and $\sim$ 0.15 μm p-GaN on the top. Under the optimum growth condition, NWs with emission wavelengths across nearly the entire visible spectral range was realized through grown on a Si substrate, and the NW diameters are in the range of 200-600 nm. The NWs have an average height $\sim$ 650 nm, with a near-perfect hexagonal morphology and smooth lateral surface. To passivate the vertical side wall of the NW, a polyimide resist layer was spin-coated onto the NW growth substrate to fully cover the NWs and then oxygen-plasma-etched to expose the NW top surface [Fig. 7(b)]. A metal electrode consisting of a Ni (10 nm)/Au (10 nm) bilayer was then deposited on the NW top surface using e-beam evaporation and then annealed at $\sim$ 500 °C for 1 min in nitrogen. It has been verified (through simulation, not shown here) that the effect of this packaging process on the mechanical properties of NW can be safely ignored.

B. Experimental Results

In the mechano-optoelectronic testing experiment, we measured the EL spectra of single InGaN/GaN NWs under different levels of contact/compression force. Fig. 8(a) shows the SEM photograph of a AFM probe tip contacting the top surface of an InGaN/GaN NW. The conductive AFM probe was employed for injecting a current of 4.2 μA into the NW; in the meanwhile, a compression force in the range of 0-5 μN was applied along the vertical direction to the NW by the AFM tip. Finally, the EL emission spectrum was collected using the emission measurement optical microfiber (Fig. 8(c)) coupled to the high-precision spectrometer.

To facilitate the control of contact force to the NW, prior to performing the real EL measurement we calibrated the relationship of the applied force level vs. the nanomanipulator displacement. Once the probe-NW contact is established, we controlled the nanomanipulator to further compress the NW and calculated the AFM tip force through the measurement method described in Section II-D. The measured force-displacement curve for a NW of 223 nm in diameter is shown Fig. 8(b). This calibration curve was used as a look-up table for applying desired contact force level to the same InGaN/GaN NW during EL characterization.

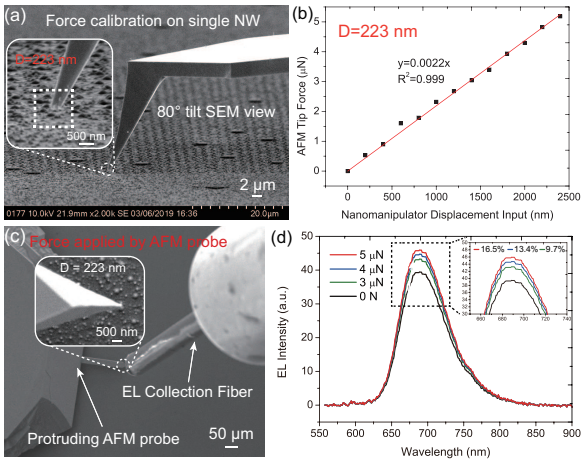

Fig. 8. Opto-electro-mechanical characterization of single InGaN/GaN NWs. (a) SEM picture of force calibration setup. (b) Force calibration result for NW with 223 nm diameter. (c) SEM picture of opto-electro-mechanical setup. (d) EL emission spectra as a function of applied compression force, for single NWs with 223 nm diameter.

Fig. 8(d) shows the EL emission spectra of the InGaN/GaN NW (diameter: 223 nm) under compression forces of 0 μN, 3 μN, 4 μN, and 5 μN. At 0 μN (gentle contact with a force level not measurable by the AFM beam deflection), the measured EL spectrum exhibits a peak emission wavelength of 686 nm, and the corresponding full width at half maximum (FWHM) of the EL spectrum is 74 nm. Once a compression force was applied to the NW top surface, the EL spectrum peak intensity increased by 9.7% at 3 μN, 13.4% at 4 μN, and 16.5% at 5 μN. This compression-induced EL enhancement of the NW could be explained by the quantum-confined Stark effect (QCSE). The compression force was applied along the growth direction of the Ga-polar single NW, and thus induced a compression strain along the c-direction and the basal plane of the InGaN/GaN wurtzite crystal structure. This compression strain decreased the piezoelectric polarization [20], which enhanced the QCSE and thus the EL peak intensity [21].

IV. Conclusion

This paper reported the development of the first SEM-based nanomanipulation system for characterizing the electrical, optical and mechanical properties of nanomaterials. With seamless integrations of multi-physical end-effectors, the system is capable of executing coupled-field nanomaterials characterization tasks. Using the developed system, we have carried out the first-time investigation of the mechanical-field impact on the EL property of single InGaN/GaN NWs, and have observed EL peak intensity enhancements for single InGaN/GaN NWs emitting red light, which has demonstrated a novel approach for reducing the QCSE of LED NWs by *in-situ* electrical nanoprobing in SEM, and paves the way for potential improvements of NWs-based nanoelectronics and optoelectronics applications.

References

[1] S. Choi, H. Lee, R. Ghaffari, T. Hyeon, and D.-H. Kim, "Recent advances in flexible and stretchable bio-electronic devices integrated with nanomaterials," *Advanced Materials*, vol. 28, no. 22, pp. 4203–4218, 2016.

[2] M. Casini, *Smart buildings: Advanced materials and nanotechnology to improve energy-efficiency and environmental performance*. Woodhead Publishing, 2016.

[3] M. You, Z. Li, P. Zhang, D. Bai, M. Lin, and F. Xu, "Nanomaterial- and micromaterial-based immunoassays," in *Handbook of Immunoassay Technologies*, pp. 273 – 304, Academic Press, 2018.

[4] H. Kim, S. Beack, S. Han, M. Shin, T. Lee, Y. Park, K. S. Kim, A. K. Yetisen, S. H. Yun, W. Kwon, *et al.*, "Multifunctional photonic nanomaterials for diagnostic, therapeutic, and theranostic applications," *Advanced Materials*, vol. 30, no. 10, p. 1701460, 2018.

[5] C. Shi, D. K. Luu, Q. Yang, J. Liu, J. Chen, C. Ru, S. Xie, J. Luo, J. Ge, and Y. Sun, "Recent advances in nanorobotic manipulation inside scanning electron microscopes," *Microsystems & Nanoengineering*, vol. 2, no. February, p. 16024, 2016.

[6] J. Qu, R. Wang, Y. Sun, I. Shih, Z. Mi, and X. Liu, "Characterizing the electrical breakdown properties of single n-i-n-n+:gan nanowires," *Applied Physics Letters*, vol. 113, no. 19, p. 193103, 2018.

[7] X. L. Wei, Q. Chen, L. M. Peng, R. Cui, and Y. Li, "In situ measurements on individual thin carbon nanotubes using nanomanipulators inside a scanning electron microscope," *Ultramicroscopy*, vol. 110, no. 3, pp. 182–189, 2010.

[8] J. B. Baxter, F. Wu, and E. S. Aydil, "Growth mechanism and characterization of zinc oxide hexagonal columns," *Applied Physics Letters*, vol. 83, no. 18, pp. 3797–3799, 2003.

[9] C. Li, M. Gao, C. Ding, X. Zhang, L. Zhang, Q. Chen, and L.-M. Peng, "In situ comprehensive characterization of optoelectronic nanomaterials for device purposes," *Nanotechnology*, vol. 20, no. 17, p. 175703, 2009.

[10] J. H. He, P. H. Chang, C. Y. Chen, and K. T. Tsai, "Electrical and optoelectronic characterization of a zno nanowire contacted by focused-ion-beam-deposited pt," *Nanotechnology*, vol. 20, no. 13, p. 135701, 2009.

[11] B. G. Yacobi and D. B. Holt, "Cathodoluminescence scanning electron microscopy of semiconductors," *Journal of Applied Physics*, vol. 59, no. 4, pp. R1–R24, 1986.

[12] A.Vila, F. F.Hernndez-Ramirez, J.Rodrłguez, O. Casals, A.Romano-Rodrłguez, J. Morante, and M. Abid, "Fabrication of metallic contacts to nanometre-sized materials using a focused ion beam (fib)," *Mater Sci Eng C*, vol. 26(5), no. 5, pp. 1063 – 1066, 2006.

[13] J. Qu, M. Lee, M. Hilke, and X. Liu, "Investigating the impact of sem chamber conditions and imaging parameters on contact resistance of in-situ nanoprobing," *Nanotechnology*, vol. 28(34), p. 345702, 2017.

[14] R. S. Gates, "Experimental confirmation of the atomic force microscope cantilever stiffness tilt correction," *Review of Scientific Instruments*, vol. 88, no. 12, p. 123710, 2017.

[15] S. Belikov, J. Alexander, C. Wall, I. Yermolenko, S. Magonov, and I. Malovichko, "Thermal tune method for afm oscillatory resonant imaging in air and liquid," in *2014 American Control Conference*, pp. 1009–1014, June 2014.

[16] S. A. Edwards, W. A. Ducker, and J. E. Sader, "Influence of atomic force microscope cantilever tilt and induced torque on force measurements," *Journal of Applied Physics*, vol. 103, no. 6, p. 064513, 2008.

[17] Y.-H. Ra, R. Navamathavan, H.-I. Yoo, and C.-R. Lee, "Single nanowire light-emitting diodes using uniaxial and coaxial ingan/gan multiple quantum wells synthesized by metalorganic chemical vapor deposition," *Nano Letters*, vol. 14, no. 3, pp. 1537–1545, 2014.

[18] A. D. L. Bugallo, L. Rigutti, G. Jacopin, F. H. Julien, C. Durand, X. J. Chen, D. Salomon, J. Eymery, and M. Tchernycheva, "Single-wire photodetectors based on ingan/gan radial quantum wells in gan wires grown by catalyst-free metal-organic vapor phase epitaxy," *Appl. Phys. Lett.*, vol. 98, no. 23, p. 233107, 2011.

[19] R. K. Debnath, R. Meijers, T. Richter, T. Stoica, R. Calarco, and H. Luth, "Mechanism of molecular beam epitaxy growth of gan nanowires on si(111)," *Appl. Phys. Lett.*, vol. 90(12), no. 12, p. 123117, 2007.

[20] W.-C. Tsai, Y.-T. Chen, C.-H. Lin, W.-T. Hsu, Y.-S. Hsu, L.-C. Chen, K.-H. Chen, and W.-H. Chang, "Suppressed piezoelectric polarization in single ingan/gan heterostructure nanowires," *Phys. Rev. B*, vol. 88, p. 155323, Oct 2013.

[21] N. Nanhui, W. Huaibing, L. Jianping, L. Naixin, X. Yanhui, H. Jun, D. Jun, and S. Guangdi, "Enhanced luminescence of ingan/gan multiple quantum wells by strain reduction," *Solid-State Electronics*, vol. 51, no. 6, pp. 860 – 864, 2007.